Optimisation of slab track design considering dynamic train–track interaction and environmental impact

Citation for the original published paper (version of record):
Aggestam, E., Nielsen, J., Lundgren, K. et al (2022). Optimisation of slab track design considering dynamic train–track interaction and environmental impact. Engineering Structures, 254. http://dx.doi.org/10.1016/j.engstruct.2021.113749

Engineering Structures 254 (2022) 113749

Contents lists available at ScienceDirect

Engineering Structures

journal homepage: www.elsevier.com/locate/engstruct

Optimisation of slab track design considering dynamic train–track interaction and environmental impact

Emil Aggestam [a,*], Jens C.O. Nielsen [a], Karin Lundgren [b], Kamyab Zandi [b], Anders Ekberg [a]

[a] Department of Mechanics and Maritime Sciences, Division of Dynamics/CHARMEC, Chalmers University of Technology, SE 412 96, Gothenburg, Sweden
[b] Department of Architecture and Civil Engineering, Division of Concrete Structures, Chalmers University of Technology, SE 412 96, Gothenburg, Sweden

ARTICLE INFO

Keywords:
Slab track
Concrete structures
Optimisation
Dynamic vehicle–track interaction
Ballastless track
Simulation
Environmental impact

ABSTRACT

Modern railway tracks for high-speed traffic are often built based on a slab track design. A major disadvantage of slab track compared to conventional ballasted track is that the environmental impact of the construction is higher due to the significant amount of concrete required. In this paper, the dimensions of the rectangular cross-sections and the types of concrete used in slab tracks are optimised with the objective to minimise greenhouse gas emissions, while considering the constraint that the design must pass the static dimensioning analysis described in the European standard 16432-2. The optimised track design is also analysed using a three-dimensional (3D) model of vertical dynamic vehicle–track interaction, where the rails are modelled as Rayleigh–Timoshenko beams and the concrete parts are represented by quadratic shell elements. Wheel–rail contact forces and the time-variant stress field of the concrete parts are calculated using a complex-valued modal superposition for the finite element model of the track. For the studied traffic scenario, it is concluded that the thickness of the panel can be reduced compared to the optimised design from the standard without the risk of crack initiation due to the dynamic vehicle load. In parallel, a model of reinforced concrete is developed to predict crack widths, the bending stiffness of a cracked panel section and to assess in which situations the amount of steel reinforcement can be reduced. To reduce the environmental impact even further, there is potential for an extended geometry optimisation by excluding much of the concrete between the rails.

1. Introduction

Railway transportation is one of the most environmentally friendly transport modes. However, a remaining environmental issue is the significant amount of greenhouse gas emissions generated by the construction of a railway track. This is especially the case for slab track where large amounts of concrete are required. If the dimensions of the slab track cross-sections and the amount of cement used could be reduced, there is a potential to reduce the environmental footprint from slab tracks significantly [1].

Today, guidelines for slab track design are given in the European standard 16432-2 [2]. For a given design, a static calculation procedure is applied to determine if the design will pass or not. In the standard, a (constant) dynamic amplification factor is used independently of train speed on the railway line. The magnitude of the dynamic effects will, however, vary depending on what track response is analysed and the quality of the track. This is not considered in the standard. Thus, to improve the guidelines for slab track design, detailed knowledge of the dynamic vehicle–track interaction is essential.

Depending on the application, a wide range of different models for vertical dynamic vehicle–track interaction has been developed [3,4]. For ballasted track, work on modelling the dynamics of track and vehicle as one coupled system started in the 1990s [5–7]. These early two-dimensional (2D) models assumed symmetry in track properties and vertical track irregularity profile with respect to the track centre line and included only one rail to save computational cost. Recently, more advanced three-dimensional (3D) slab track models have been developed. One of the first 3D models was developed by Zhai et al. [8]. In their work, where the concrete panels were modelled as elastic rectangular plates, non-symmetric dynamic excitation was considered. In several studies, cf. [8–14], 3D slab track models have been validated against measurements. The main drawback of using a 3D model is that the computational cost is increased, and it can therefore be beneficial to use a 2D model in situations where several simulations need to be performed, e.g. when simulating long-term differential track settlement [15] or optimising the track design [16]. In several papers, comparisons between 2D and 3D models have been performed to

---

* Corresponding author.
E-mail addresses: emil.aggestam@chalmers.se (E. Aggestam), jens.nielsen@chalmers.se (J.C.O. Nielsen), karin.lundgren@chalmers.se (K. Lundgren), kamyab.zandi@chalmers.se (K. Zandi), anders.ekberg@chalmers.se (A. Ekberg).

https://doi.org/10.1016/j.engstruct.2021.113749
Received 30 June 2021; Received in revised form 16 November 2021; Accepted 7 December 2021

investigate in which situations a 2D model is sufficient and in which conditions a 3D model is required [9,17].

The number of reported strength analyses of concrete structures related to railway research is relatively limited. In a paper by Poveda et al. [18], fatigue due to compressive loads on the concrete panel was considered. The magnitude of stress intensity factors when considering a through-transverse crack in the roadbed was studied by Zhu et al. [19]. In their analysis, a simplified 3D model consisting of beam and plate elements was used to calculate the wheel–rail contact forces. The calculated forces were then applied as input to a more detailed finite element model of the track, where the panel, CA (concrete-asphalt) mortar, roadbed and subgrade were all modelled by solid elements. By using the extended finite element method (XFEM), stress intensity factors at the crack tip in the concrete roadbed could be determined. Milford and Allwood [20] studied the environmental impact from different types of tracks including emissions from materials, processes and transport associated with construction, maintenance and end-of-life activities. From their study, it was concluded that the environmental impact could be reduced significantly by using an embedded rail design over a ballasted track design. Hahrs et al. [21] used theory based on the European standard 16432-2 [2] and Eurocode 2 [22] and conducted parametric studies to investigate the impact of the soil stiffness on different track responses. By including stochastic variables in a ballasted track model, Rahrovani [23] studied how statistical methods can be used to calculate the probability of failure (PF) of a concrete monobloc sleeper. Based on multiple simulations of vehicle–track dynamics, the PF was determined using either Markov chain or Monte Carlo simulations. By using the Nelder–Mead method, the parameter values for the stochastic variables that resulted in a predefined PF-value could be determined. The PF was also studied by Tarifa et al. [24]. From compressive fatigue tests on cubic specimens, the parameters used to calculate the PF were calibrated. Furthermore, three-point bending tests on full-scale concrete slabs were conducted and a novel approach to detect critical damage of the slabs was developed. Rezaie et al. [25] used both numerical and experimental analyses to investigate longitudinal cracks in pre-stressed concrete sleepers. In their model, the concrete was represented by solid elements while the steel bars were described by truss elements. Zi et al. [26] developed a non-linear finite element model to study conical crack formations in concrete sleepers in a slab track system. In compression, the concrete was modelled as a linear elastic material, while a softening plasticity model including a cohesive crack model was used in tension. You et al. [27] presented a review of fatigue life assessment methods for prestressed concrete sleepers. In their paper, it was concluded that the fatigue life of sleepers is typically assessed by estimating the dynamic loads and support conditions for the sleeper and calculating the bending moment at critical sections.

In this paper, a slab track design that minimises the greenhouse gas emissions is derived while considering the constraint that the design must pass the European standard 16432-2 [2]. Based on the optimised design, simulations of vertical dynamic vehicle–track interaction are then performed, and it is shown that the design can be trimmed even further. By taking the dynamics of the track into account, novel recommendations for next-generation slab track structures are presented. In these simulations, both cracked and uncracked sections of the concrete panel are considered, and the influence of cracks in the concrete panel on track responses at several operational scenarios is determined. The characteristics of a cracked section, which is used as input to the dynamic model, is determined using a model of reinforced concrete. By using the maximum bending moment calculated with the linear dynamic model as input to the non-linear model of reinforced concrete, crack widths are calculated which are compared with criteria in the existing standard, see Ref. [28]. Finally, the model of reinforced concrete is also used to assess if the amount of steel reinforcement in the slab track design can be reduced, which may lead to additional carbon dioxide (CO_2) savings.

2. European standard for slab track design — Static analysis

The criteria for slab track design are given in the European standard 16432-2 [2]. In particular, a static calculation method is presented for the design of different types of slab tracks. The considered designs include both single and multiple layers of concrete. In this paper, the focus is on two-layered concrete structures since this seems to be the most commonly used design. The upper concrete layer is assumed to be a prefabricated slab, referred to as the panel, while the lower layer is taken as a Hydraulically Bound Layer (HBL), referred to as the roadbed. For two-layered concrete structures, two calculation methods are presented, either with no or full bond between the panel and roadbed. In this paper, the calculation method which assumes full bond is used, see Section 2.1, since the optimal solution assuming no bond converged to a single-layer structure which is not the focus of this paper.

2.1. General description of the calculation method

The basis of the analytical design calculation method is to compare calculated stresses with strength limits. The analytical calculations can be divided into three parts representing the design criteria for the rail, the concrete parts and the substructure, respectively. In this paper, which focuses on the environmental impact of building slab track, the design criteria for the concrete parts are studied in detail.

The calculation method for the slab design is summarised in Fig. 1. In the initial step, data settings for vehicle load, concrete parts and temperature load have to be defined. The vehicle load times a dynamic amplification factor of 1.5 (independently of design train speed) is then used in a beam model of the rail to calculate the rail seat loads. The obtained rail seat loads are then applied to both a beam and a slab model of the concrete parts. From these models, flexural stresses are calculated (in the longitudinal direction for the beam model and both the lateral and longitudinal directions for the slab model). In the longitudinal direction, a conservative approach is used by selecting the maximum calculated flexural stress from the beam and slab models. The calculated flexural stresses are then compared with the corresponding flexural strength limits from a fatigue model. In this paper, the values for the temperature loads used in the fatigue model are taken from the standard [2]. By taking the ratios of the flexural strength limits and the corresponding flexural stresses, different safety factors (SFs) are determined. If all of the calculated safety factors are larger than or equal to one, the design is approved.

2.2. Optimisation of track based on the standard

For the optimised slab track design, there is a trade-off between cost and performance. In this paper, the track is optimised to minimise the amount of emitted CO_2 while fulfilling the requirements in the European standard 16432-2 [2]. When concrete is manufactured, the cement stands for roughly 85% of the CO_2 emissions. The remaining 15% is neglected in the present optimisation.

The amount (kilogrammes) of cement in the slab track structure is determined by multiplying the volume of concrete by the amount of cement per cubic metre. In this paper, three different concrete classes are considered: a low-quality concrete (C25/30), a concrete type that is commonly used in monobloc sleepers (C40/50), and a high-performance concrete (C50/60). The amount of cement per cubic metre for these three concrete types are $c_{\mathrm{l}} = 290$ kg/m^3, $c_{\mathrm{m}} = 390$ kg/m^3 and $c_{\mathrm{h}} = 430$ kg/m^3, where subscripts l, m and h stand for low, medium and high-quality concrete. For the roadbed, it is stated in the European standard 16432-2 [2] that this layer should have at least 3% cement. Thus, assuming that the roadbed has a density of 2400 kg/m^3, the amount of cement per cubic metre in the roadbed is set to $c_{\mathrm{r}} =$ 72 kg/m^3. Finally, an environmentally optimised type of cement is considered, which emits $\alpha_{\mathrm{c}} = 0.678$ kg CO_2 per kg cement [29].

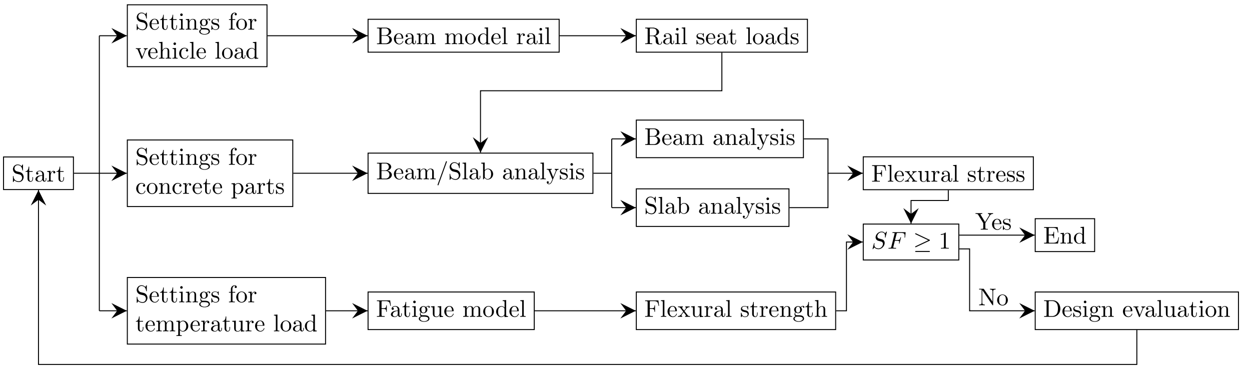

Fig. 1. Steps in the analytical calculation model for the concrete parts presented in the European standard 16432-2 [2].

For each type of concrete, the minimisation of CO_2 emissions per metre slab track can be written as

$$\begin{aligned} &f_i = \min \alpha_c (c_i w_1 t_1 + c_r w_2 t_2), \quad i = \{\mathrm{l}, \mathrm{m}, \mathrm{h}\}, \\ &\text{subject to } \boldsymbol{w} \in S^{\mathrm{w}},\ \boldsymbol{t} \in S^{\mathrm{t}},\ SF_j \geq 1, \forall j = 1, 2, \ldots, n_{\mathrm{SF}}, \end{aligned} \tag{1}$$

where $\boldsymbol{w}$ and $\boldsymbol{t}$ are vectors containing the widths and thicknesses of the rectangular panel and roadbed, see Fig. 2, $S^{\mathrm{w}} \subset \mathbb{R}^2$ and $S^{\mathrm{t}} \subset \mathbb{R}^2$, while SF_j are the values of each safety factor used in the standard and n_{SF} is the number of safety factors. The sets S^{w} and S^{t} are defined as

$$\begin{aligned} S^{\mathrm{w}} &= \{\boldsymbol{w} \in \mathbb{R}^2 :\ w_i \geq w_{\mathrm{L},i}\ \forall\, i = 1, 2\}, \\ S^{\mathrm{t}} &= \{\boldsymbol{t} \in \mathbb{R}^2 :\ t_i \geq 0\ \forall\, i = 1, 2\}, \end{aligned} \tag{2}$$

where $w_{\mathrm{L},i} = [w_{\mathrm{L},1},\ w_{\mathrm{L},2}]$ is the lower limit of the widths of the panel and roadbed. In this paper, the widths $w_{\mathrm{L},1} = 2.6$ m and $w_{\mathrm{L},2} = 3.2$ m are used based on the recommendations given in Appendix C in the European standard 16432-2 [2].

The optimal design can be obtained by simply taking the minimum amount of CO_2 emissions for all compared concrete types as

$$f_{\mathrm{opt}} = \min_{i=\{\mathrm{l},\mathrm{m},\mathrm{h}\}} f_i. \tag{3}$$

Note that the cost function described in Eq. (1) assumes that there are two layers of bound materials. The corresponding objective function for a single-layered design can be obtained by simply omitting the second term in the objective function. The optimised design is presented and discussed in Section 5.

3. Model of dynamic vehicle–track interaction

The performance of the optimised slab track design is further analysed using a linear 3D model of vertical dynamic vehicle–track interaction. The 3D track model has been calibrated and validated against measurements in a full-scale test rig [10]. In Fig. 2, a schematic cross-section of the 3D track model is shown. The rails are modelled using Rayleigh–Timoshenko beams with bending stiffness $EI_{\mathrm{r}} = 6.4$ MNm^2, shear stiffness $kGA_{\mathrm{r}} = 250$ MN, mass $m_{\mathrm{r}} = 60$ kg/m per unit beam length and rotatory inertia $m_{\mathrm{r}} r_{\mathrm{r}}^2 = 0.24$ kgm per unit beam length. The rail seat distance is $l = 0.65$ m and the concrete parts are described using shell elements with density $\rho_{\mathrm{s}} = 2400$ kg/m^3 and Poisson's ratio $\nu_{\mathrm{s}} = 0.15$. The modulus of elasticity and the tensile and compressive strengths will vary depending on what type of concrete is used, see Section 4.2. In this study, shell elements are chosen over solid elements since they are computationally faster to use and from the shell elements, it is straightforward to determine the bending moment which is needed in the post-processing calculation of the steel stresses. Since also stresses in the concrete will be calculated, a quadratic element is preferred, cf. [17], and thus the quadratic element denoted S8R in Abaqus [30] is used.

The roadbed is modelled as a continuous hydraulically bound layer, while each concrete panel is modelled as a discrete concrete slab with a length corresponding to eight rail seat distances. The influence of the extra amount of concrete used at each rail seat is neglected. From dynamic simulations, it was verified that including this extra concrete at each rail seat, similar as in Ref. [17], would not affect the considered track responses significantly.

Table 1
Stiffness and viscous damping of resilient layers in the track model.

Stiffness	$k_{\mathrm{f}} = 100$ MN/m^3	$k_{\mathrm{s}_1/\mathrm{s}_2} = 1.0$ GN/m^3	$k_{\mathrm{r}/\mathrm{s}_1} = 34$ kN/mm
Damping	$c_{\mathrm{f}} = 82$ kNs/m^3	$c_{\mathrm{s}_1/\mathrm{s}_2} = 250$ kNs/m^3	$c_{\mathrm{r}/\mathrm{s}_1} = 5.8$ kNs/m

The rail pads, soil, and layer between the concrete parts are modelled as non-interacting springs and viscous dampers. To reduce spurious stress concentrations in the panel, each rail pad is modelled as a set of springs and viscous dampers acting in parallel that distributes the load from the rail over an area corresponding to the area of the rail pad, see Fig. 3. The parameter values for each layer are shown in Table 1. The stiffness and viscous damping per unit area of the foundation are denoted k_{f} and c_{f}, the stiffness and viscous damping of each rail pad are denoted $k_{\mathrm{r}/\mathrm{s}_1}$ and $c_{\mathrm{r}/\mathrm{s}_1}$, whereas the stiffness and viscous damping per unit area of the layer between the panel and roadbed are denoted $k_{\mathrm{s}_1/\mathrm{s}_2}$ and $c_{\mathrm{s}_1/\mathrm{s}_2}$. The parameter values of $k_{\mathrm{s}_1/\mathrm{s}_2}$ and $c_{\mathrm{s}_1/\mathrm{s}_2}$ were obtained based on a commercially used slab track design, which uses a thin rubber mat of thickness 3 mm between the concrete parts. The stiffness of this slab mat is around 1.0 GN/m^3. The damping per unit area of $c_{\mathrm{s}_1/\mathrm{s}_2}$ was determined by assuming a similar k/c-ratio as for the rail pad. In order to avoid rigid body motions (RBMs) of the panels and to include the shear effect of the bond between panel and roadbed, the springs that connect the panels to the roadbed act in all three spatial dimensions. In Ref. [17], it was concluded that the springs in the lateral and longitudinal directions have a negligible effect on the vertical dynamics of the track. It has been verified that the employed soil stiffness yields similar values of the modulus of deformation, $E_{\mathrm{v}2}$, as presented in the European standard 16432-2 [2]. The soil damping, c_{f}, was selected by assuming a similar ratio between stiffness and viscous damping as for the corresponding values specified by Nielsen [31]. Finally, the rail pad stiffness $k_{\mathrm{r}/\mathrm{s}_1}$ and viscous damping $c_{\mathrm{r}/\mathrm{s}_1}$ were obtained from the calibration of the track model against hammer impact measurements in a test rig [10].

The computational demands when using a 3D dynamic model may be significant. From the convergence analyses reported in Ref. [17], it was found that the influences of boundary effects and transients induced by the start of the simulation on the calculated responses at the centre of the track model were negligible if the length of the track model was at least 120 rail seat distances. Furthermore, to reduce the computational cost, it was concluded that the first and final third of the concrete parts in the track model could be modelled by beam elements instead of shell/solid elements without affecting the track responses at the centre of the track model. Therefore, a track model with a total length of 78 m is used, corresponding to 120 rail seat distances,

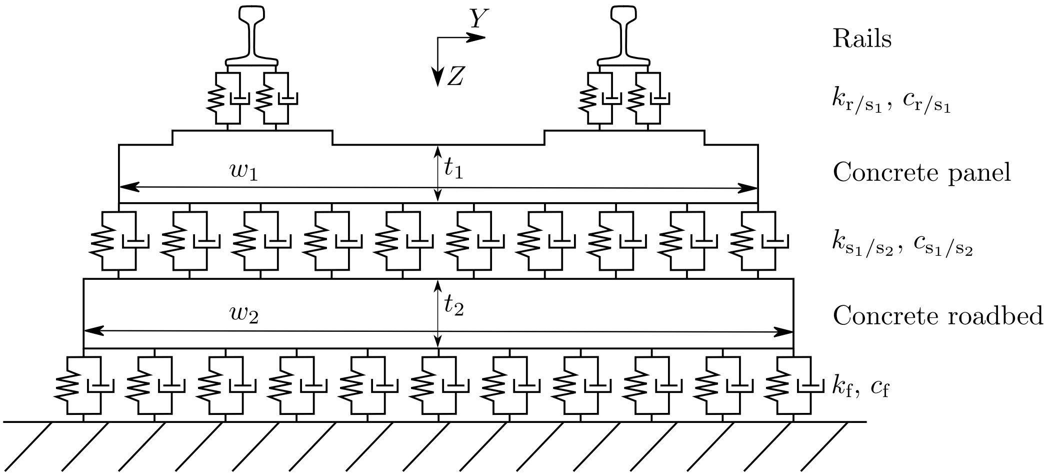

Fig. 2. Schematic cross-section of the 3D track model.

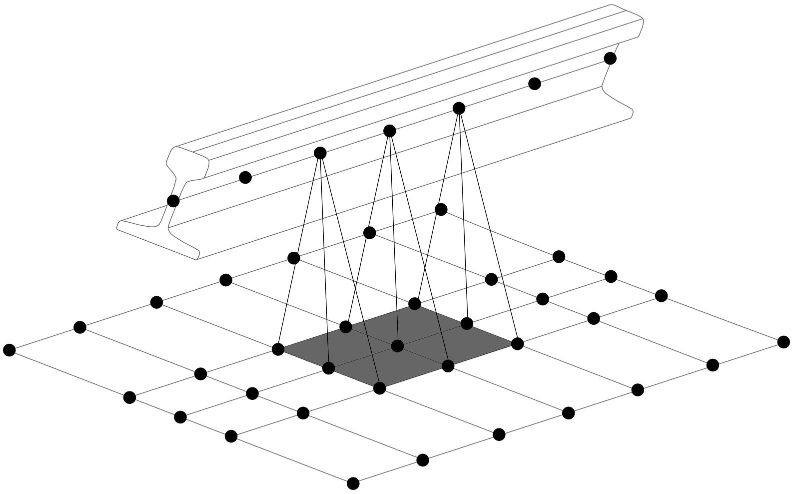

Fig. 3. Sketch of the rail pad model. Each line connecting the rail and the panel includes a spring and a viscous damper acting in the vertical direction. The shaded area corresponds to the area of the rail pad that is in contact with the bottom area of the rail.

where the concrete parts are described by shell elements only in the middle third of the track model. The connection between the beam and shell elements of the concrete parts are modelled using a multipoint constraint (MPC) and is described in detail in Ref. [17]. Regarding mesh discretisation, an average element length of 11 cm is used, which is fine enough according to the convergence study presented in Ref. [17].

The vehicle is modelled as a multibody system and is illustrated in Fig. 4. The 3D vehicle model is representing a bogie containing two wheelsets, primary suspensions and a bogie frame. The influence of the car body is accounted for by a constant vertical point load acting at the centroid of the bogie. For the track responses considered in this paper, a more advanced vehicle model is not required since the secondary suspension acts as a dynamic filter in the frequency range where the track dynamics is significant [3]. A comparison of different vehicle models in terms of track responses which are of interest in this paper was presented in Ref. [16].

The 3D vehicle model has eleven degrees of freedom (DOFs). Seven of the DOFs, denoted $\boldsymbol{x}^{\mathrm{v}}_{\mathrm{b}}$, are used to model the vertical and roll motions of each wheelset and the vertical, roll and pitch motions of the bogie frame. The remaining four DOFs, denoted $\boldsymbol{x}^{\mathrm{v}}_{\mathrm{a}}$, have no mass and are used in the constraint equation to couple the vehicle and track models. The equations of motion for the vehicle model can be written as

$$\begin{bmatrix}\mathbf{0} & \mathbf{0}\\ \mathbf{0} & \boldsymbol{M}^{\mathrm{v}}_{\mathrm{bb}}\end{bmatrix}\begin{Bmatrix}\ddot{\boldsymbol{x}}^{\mathrm{v}}_{\mathrm{a}}(t)\\ \ddot{\boldsymbol{x}}^{\mathrm{v}}_{\mathrm{b}}(t)\end{Bmatrix}+\begin{bmatrix}\mathbf{0} & \mathbf{0}\\ \mathbf{0} & \boldsymbol{C}^{\mathrm{v}}_{\mathrm{bb}}\end{bmatrix}\begin{Bmatrix}\dot{\boldsymbol{x}}^{\mathrm{v}}_{\mathrm{a}}(t)\\ \dot{\boldsymbol{x}}^{\mathrm{v}}_{\mathrm{b}}(t)\end{Bmatrix}$$
$$+\begin{bmatrix}\boldsymbol{K}^{\mathrm{v}}_{\mathrm{aa}} & \boldsymbol{K}^{\mathrm{v}}_{\mathrm{ab}}\\ \boldsymbol{K}^{\mathrm{v}}_{\mathrm{ba}} & \boldsymbol{K}^{\mathrm{v}}_{\mathrm{bb}}\end{bmatrix}\begin{Bmatrix}\boldsymbol{x}^{\mathrm{v}}_{\mathrm{a}}(t)\\ \boldsymbol{x}^{\mathrm{v}}_{\mathrm{b}}(t)\end{Bmatrix}+\begin{Bmatrix}\boldsymbol{F}_{\mathrm{a}}(t)\\ \mathbf{0}\end{Bmatrix}=\begin{Bmatrix}\mathbf{0}\\ \boldsymbol{F}^{\mathrm{ext}}_{\mathrm{b}}\end{Bmatrix}, \tag{4}$$

where $\boldsymbol{F}_{\mathrm{a}}(t)$ contains the wheel–rail contact forces and $\boldsymbol{F}^{\mathrm{ext}}_{\mathrm{b}}$ contains all external loads (in this study only gravity loads). The expression of each matrix in Eq. (4) can be found in Appendix A in Ref. [17]. The wheel–rail contact is modelled as Hertzian, where the contact stiffness between each wheel and rail is given by

$$k_{\mathrm{H}i}=C_{\mathrm{H}}\langle x_{\mathrm{b}i}-x_{\mathrm{a}i}\rangle^{1/2},\quad i=1,2,3,4. \tag{5}$$

Here, C_{H} is the Hertzian constant and the Macaulay brackets are defined as $\langle\bullet\rangle=\frac{1}{2}(\bullet+|\bullet|)$. In this paper, a vehicle speed of 250 km/h is considered (except in Fig. 8 where the effect of increasing speed is investigated).

The input data for the vehicle model, presented in Table 2, was collected from Ref. [32]. The mass of the car body has, however, been modified such that an axle load of 17 tonnes is achieved (except in Figs. 6(b) and 7 where the effect of varying the axle load is investigated). In Table 2, the masses M_{b}, M_{w} and M_0 denote the masses of the bogie, wheelset and half of the car body, respectively, J_{br} and J_{bp} denote the roll and pitch inertias of the bogie, while J_{wr} denotes the roll

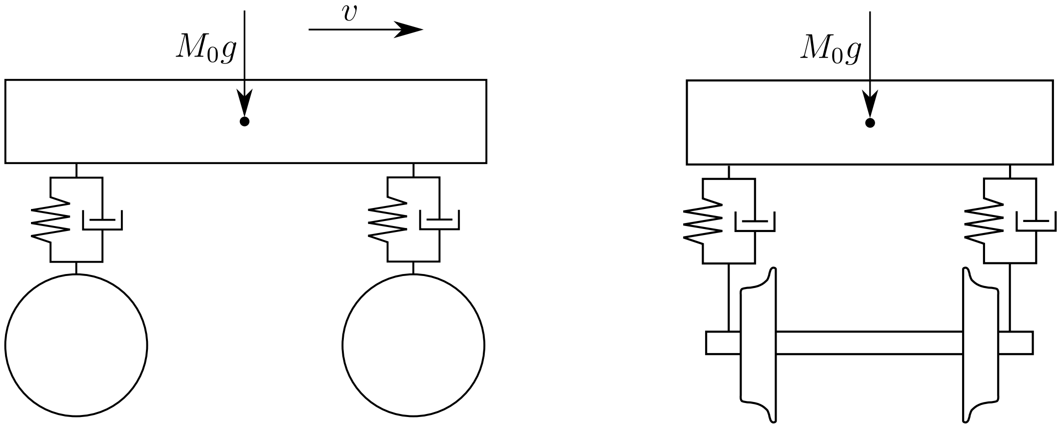

(a) (b)

Fig. 4. Sketch of vehicle model. (a) Side view and (b) end view. M_0 corresponds to the mass of half of the car body.

Table 2
Parameter values used in the vehicle model collected from Ref. [32] (except M_0).

$M_b = 2.6$ tonnes	$M_w = 1.8$ tonnes	$M_0 = 28$ tonnes
$J_{br} = 1700$ kgm^2	$J_{bp} = 1500$ kgm^2	$J_{wr} = 1100$ kgm^2
$L = 0.75$ m	$d = 1.28$ m	$\Delta = 1.00$ m
$k = 1200$ kN/m	$c = 4$ kNs/m	

inertia of the wheelset. The length L denotes the lateral distance from the centre of the track to the running circle of the wheel tread, whereas d and Δ denote the distances from the bogie centre to the primary suspension in the longitudinal and lateral directions. Finally, k and c denote the stiffness and viscous damping of the primary suspension.

The track model is developed in Abaqus using Python scripts, which facilitates parametric studies considering different track models with varying mesh densities, dimensions and material properties. By running the Python scripts in Abaqus, the stiffness, damping and mass matrices of the track, $\boldsymbol{K}^{\mathrm{t}}$, $\boldsymbol{C}^{\mathrm{t}}$ and $\boldsymbol{M}^{\mathrm{t}}$, are generated. These matrices are exported to Matlab where the dynamic vehicle–track interaction is simulated using an in-house software.

The computational cost of the dynamic simulation is reduced by introducing the corresponding complex-valued modal solution of the equations of motion for the linear track model as

$$\begin{bmatrix} \boldsymbol{K}^{\mathrm{t}^{-1}}\boldsymbol{C}^{\mathrm{t}} & \boldsymbol{K}^{\mathrm{t}^{-1}}\boldsymbol{M}^{\mathrm{t}} \\ -\mathbf{I} & \mathbf{0} \end{bmatrix} \begin{Bmatrix} \underline{\boldsymbol{\rho}}^{(n)} \\ \mathrm{i}\underline{\omega}_n\underline{\boldsymbol{\rho}}^{(n)} \end{Bmatrix} = -\frac{1}{\mathrm{i}\underline{\omega}_n} \begin{Bmatrix} \underline{\boldsymbol{\rho}}^{(n)} \\ \mathrm{i}\underline{\omega}_n\underline{\boldsymbol{\rho}}^{(n)} \end{Bmatrix}, \qquad (6)$$

where $\underline{\omega}_n$ are the angular eigenfrequencies, $\underline{\boldsymbol{\rho}}^{(n)}$ the eigenvectors, $\mathbf{I}$ denotes the unit matrix and underline indicates a complex-valued quantity. The computational cost is reduced by only including modes in the dynamic solution which has a corresponding eigenfrequency below a predefined threshold value (in this study 1000 Hz). It has been verified that the influence of the truncated modes on the considered track responses is negligible [17].

The modal representation of the track model is coupled with the equations of motion of the vehicle model by using the constraint that the DOFs in $\boldsymbol{x}_{\mathrm{a}}^{\mathrm{v}}$ are interfacing with the track [5,33]. A mixed extended state-space vector $\underline{\boldsymbol{z}}$ is defined as

$$\underline{\boldsymbol{z}} = \{\underline{\boldsymbol{q}}^{\mathrm{tT}} \quad \boldsymbol{x}_{\mathrm{a}}^{\mathrm{vT}} \quad \boldsymbol{x}_{\mathrm{b}}^{\mathrm{vT}} \quad \dot{\boldsymbol{x}}_{\mathrm{a}}^{\mathrm{vT}} \quad \dot{\boldsymbol{x}}_{\mathrm{b}}^{\mathrm{vT}} \quad \hat{\boldsymbol{F}}_{\mathrm{a}}^{\mathrm{T}}\}^{\mathrm{T}}, \qquad (7)$$

where the complex-valued modal displacements of the track model are denoted $\underline{\boldsymbol{q}}^{\mathrm{t}}$, while $\hat{\boldsymbol{F}}_{\mathrm{a}} = \int \boldsymbol{F}_{\mathrm{a}}(t)\mathrm{d}t$. This state-space vector is used to derive a coupled, time-variant system which is given by

$$\underline{\boldsymbol{A}}(\underline{\boldsymbol{z}}, t)\dot{\underline{\boldsymbol{z}}} + \underline{\boldsymbol{B}}(\underline{\boldsymbol{z}}, t)\underline{\boldsymbol{z}} = \underline{\boldsymbol{F}}(\underline{\boldsymbol{z}}, t), \qquad (8)$$

where the vector $\underline{\boldsymbol{F}}$ and the matrices $\underline{\boldsymbol{A}}$ and $\underline{\boldsymbol{B}}$ are defined in Eq. (15) in Ref. [33]. From Eq. (8), a generic initial value problem is derived, where $\underline{\boldsymbol{z}}(t)$ can be solved (numerically) in the time domain. This simulation methodology, which is used to calculate the wheel–rail contact forces, has previously been validated for ballasted track [31]. For more information about the track model and the simulation methodology, see Refs. [5,17,31,33].

By differentiating the calculated state-space vector, the time history of the wheel–rail contact force at each wheel can be determined. These wheel–rail contact forces are used as input to a post-processing simulation in Abaqus to determine the time-varying stress field in the concrete parts. By combining the time history of the wheel–rail contact forces and the shape functions derived from Rayleigh–Timoshenko beam theory, the forces and moments that shall be applied to each rail DOF in each time step are calculated. The post-processing simulation in Abaqus is performed using the so-called modal dynamic approach, which is a valid and applicable option since the track model is taken as linear. Results from simulations with the dynamic model are presented in Section 5.

4. Model of reinforced concrete

Cracks forming in the concrete parts of a slab track can weaken the structural integrity and introduce a risk for reinforcement corrosion. In this paper, a model of the concrete panel has been developed. The panel is assumed to be a prefabricated double-reinforced slab without any embedded sleepers. Note that there is no need to develop a similar model for the roadbed since it is a hydraulically bound layer without any reinforcement.

Depending on the application and which concrete response needs to be captured, different modelling strategies can be used spanning from simple hand calculation models to advanced 3D non-linear FE-models [34]. In this paper, the purpose of the reinforced concrete model is to calculate the bending stiffness of a cracked panel section, the stress in the steel reinforcement and the crack widths. These responses are estimated from a beam model, where uniaxial stress-state and full interaction between concrete and steel are assumed. Since full bond is assumed, the reinforcement bars can, in the simulation model, be replaced with concrete with a transformed cross-section. Linear elastic models are assumed for the concrete in compression and for the steel in both compression and tension. Finally, note that if other responses, e.g. the crack pattern, should be analysed, more advanced models are needed where the bond–slip between steel and concrete is taken into account.

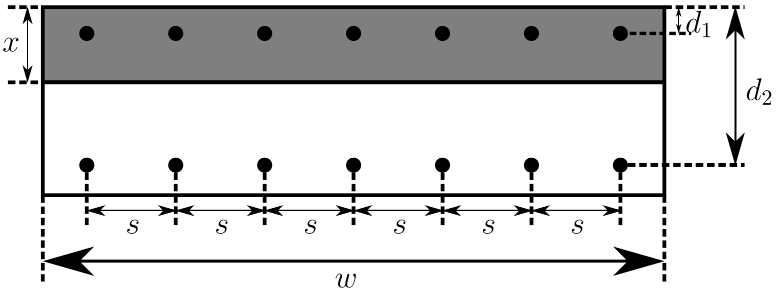

Fig. 5. Sketch of the cross-section of the panel used in the model of reinforced concrete. The shaded area indicates concrete in compression.

4.1. Bending stiffness of a cracked section

The location of the neutral axis is established by neglecting the influence of the concrete in tension and by assuming full bond between concrete and reinforcement for the cracked section. For calculations where long-term effects are taken into account, the so-called effective modulus of elasticity, $E_{\mathrm{c,eff}}$, and the effective modular ratio, β, are required. In this paper, these properties are calculated following Eurocode 2 [22] as

$$E_{\mathrm{c,eff}} = \begin{cases} E_{\mathrm{c}} & \text{short term,} \\ \frac{E_{\mathrm{c}}}{1+\varphi(\infty,t_0)} & \text{long term,} \end{cases} \tag{9}$$

$$\beta = \frac{E_{\mathrm{s}}}{E_{\mathrm{c,eff}}}, \tag{10}$$

where $\varphi(\infty, t_0)$ is the final creep value and E_{s} and E_{c} are the elastic moduli of the steel and concrete, respectively. In addition, the same cross-sectional area, A_{s}, of both the upper and lower reinforcement bars is used, and the same distance, s, is assumed between the reinforcement bars in the lateral and longitudinal directions.

In Fig. 5, the cross-section of the panel is shown. When considering a cracked double-reinforced section and assuming that the neutral axis coincides with the centre of gravity, the distance, x, from the top of the panel to the neutral axis can be found by solving, [35],

$$w\left[\frac{x^2}{2} + \frac{(\beta-1)A_{\mathrm{s}}(x-d_1)}{s} - \frac{\beta A_{\mathrm{s}}(d_2-x)}{s}\right] = 0, \tag{11}$$

where w is the width of the slab and d_1 and d_2 are the distances from the top of the panel to the upper and lower reinforcements. The effective area, A_{eff}, and the effective moment of inertia, I_{eff}, of the concrete and steel when the steel cross-section has been transformed are then obtained as

$$A_{\mathrm{eff}} = w[x + (\beta-1)A_{\mathrm{s}}/s + \beta A_{\mathrm{s}}/s], \tag{12a}$$

$$I_{\mathrm{eff}} = w[x^3/3 + (\beta-1)A_{\mathrm{s}}(x-d_1)^2/s + \beta A_{\mathrm{s}}(d_2-x)^2/s]. \tag{12b}$$

4.2. Crack widths

To estimate crack widths, the steel stresses need to be estimated. To this end, the shrinkage load, F_{cs}, is calculated as, [35],

$$F_{\mathrm{cs}} = E_{\mathrm{s}}\epsilon_{\mathrm{cs},\infty}A_{\mathrm{s}}w/s, \tag{13}$$

where $\epsilon_{\mathrm{cs},\infty}$ is the total final shrinkage strain, which in this paper is calculated following Eurocode 2 [22]. Note that this shrinkage load acts both at the upper and lower reinforcements.

From the applied bending moment, M, and the shrinkage load, the concrete stress at location z measured from the neutral axis can be determined by Navier's formula as

$$\sigma_{\mathrm{c},\infty}(z) = \frac{2F_{\mathrm{cs}}}{A_{\mathrm{eff}}} + \frac{F_{\mathrm{cs}}(e_{\mathrm{s1,eff}} + e_{\mathrm{s2,eff}}) + M}{I_{\mathrm{eff}}}z, \tag{14}$$

Table 3
Concrete input data for the reinforced concrete model.

	f_{cm} [MPa]	f_{ck} [MPa]	f_{ctm} [MPa]	E_{c} [GPa]	$\epsilon_{\mathrm{cd},0}$ [–]
C25/30	33	25	2.6	31	$2.9 \cdot 10^{-4}$
C40/50	48	40	3.5	35	$2.4 \cdot 10^{-4}$
C50/60	58	50	4.1	37	$2.1 \cdot 10^{-4}$

where $e_{\mathrm{s1,eff}} = d_1 - x$ and $e_{\mathrm{s2,eff}} = d_2 - x$. The steel stress in the tensile reinforcement assuming a cracked section is then calculated as

$$\sigma_{\mathrm{s}} = -\frac{F_{\mathrm{cs}}s}{A_{\mathrm{s}}w} + \beta\sigma_{\mathrm{c},\infty}(e_{\mathrm{s2,eff}}), \tag{15}$$

According to Eurocode 2 [22], the difference between the mean strain in the reinforcement and the mean strain of the concrete between the cracks can be written as

$$\Delta\epsilon_{\mathrm{m}} = \max\left(\frac{\sigma_{\mathrm{s}} - k_{\mathrm{t}}\frac{f_{\mathrm{ctm}}}{\rho_{\mathrm{p,eff}}}(1+\beta\rho_{\mathrm{p,eff}})}{E_{\mathrm{s}}},\ 0.6\frac{\sigma_{\mathrm{s}}}{E_{\mathrm{s}}}\right), \tag{16}$$

where k_{t} is a factor depending on whether the loading is short-term or long-term, f_{ctm} is the mean axial tensile strength of the concrete, $\rho_{\mathrm{p,eff}} = A_{\mathrm{s}}/(sA_{\mathrm{t}})$ and A_{t} is the effective area of the concrete in tension surrounding the reinforcement at depth

$$t_{1,\mathrm{eff}} = \min\left[2.5(t_1 - d_2), (t_1 - x)/3, t_1/2\right]. \tag{17}$$

Finally, the crack width, w_{k}, can be calculated as

$$w_{\mathrm{k}} = s_{\mathrm{r,max}}\Delta\epsilon_{\mathrm{m}}, \tag{18}$$

where $s_{\mathrm{r,max}}$ is the characteristic crack spacing given as

$$s_{\mathrm{r,max}} = k_3c + k_1k_2k_4\frac{\phi}{\rho_{\mathrm{p,eff}}}. \tag{19}$$

Here, ϕ is the diameter of the reinforcement bar, c is the thickness of the concrete cover and k_1, k_2, k_3 and k_4 are parameter values which vary with the reinforcement surface and type of loading. Input data for the concrete and steel is presented in Tables 3 and 4.

It should be noted that the magnitudes of the steel stresses and crack widths are independent of the width of the section since the shrinkage load, effective area and moment of inertia are all varying linearly with the width of the section. The applied bending moment, which is calculated from the dynamic model presented in Section 3, expresses the bending moment calculated per metre. In order to be consistent, the width in the reinforced concrete model is therefore set to one metre, and all responses are calculated per metre width.

4.3. Influence of external restraint forces

The calculations above neglect the influence of external restraint forces. For the concrete panel in a slab track, it is difficult to determine the external restraint degree, which may vary between different designs. The approach taken here is to repeat the calculations with either no external restraint or full external restraint to obtain the bounds.

Table 4
Steel input data for the reinforced concrete model.

$E_s = 210$ GPa	$f_{ys} = 500$ MPa	$f_u = 540$ MPa	$\rho_s = 7800$ kg/m^3	$\phi = 20$ mm	$s = 140$ mm

Table 5
Results from the optimisation problem based on the European standard 16432-2 [2] when using an axle load of 17 tonnes.

	CO_2 [kg/m]	t_1 [cm]	w_1 [m]	t_2 [cm]	w_2 [m]
C25/30	137	19	2.6	26	3.2
C40/50	147	18	2.6	15	3.2
C50/60	152	18	2.6	9.0	3.2

These extreme external restraints correspond to a situation where the panel is either completely free to move or that movements are fully prevented (typically due to surrounding structures).

When full external restraint is assumed, the steel stress due to the external restraint, $\sigma_{s,res}$, can be estimated using the following deformation condition, [36],

$$\frac{\sigma_{s,res}A_s + F_{cs}}{E_{c,eff}A_{I,eff}}l_{res} + n_{cr}w_{m,c}(\sigma_{s,res}) - \epsilon_{cs}l_{res} = 0, \tag{20}$$

where l_{res} is the length between the external restraints, n_{cr} is the number of cracks between the external restraints and $w_{m,c}$ is the crack width when having cyclic or sustained loading and taking long-term effects into account. Based on a stress–slip relation for long-term response, cf. [37], a conservative estimation of $w_{m,c}$ is given by, [36],

$$w_{m,c} = 0.52\left(\frac{\phi\sigma_{s,res}^2}{0.22f_{cm}E_s}\right) + \frac{4\sigma_{s,res}\phi}{E_s}. \tag{21}$$

The steel stress contribution due to the external restraint is calculated using an iterative approach. By initially setting $n_{cr} = 1$, $\sigma_{s,res}$ is evaluated using Eqs. (20)–(21). The total steel stress when assuming full external restraint, $\sigma_{s,tot}$, can then be calculated as

$$\sigma_{s,tot} = \sigma_s + \sigma_{s,res}. \tag{22}$$

From the total steel stress, the external restraint force, F_{res}, is calculated as

$$F_{res} = \frac{\sigma_{s,tot}A_s w}{s}. \tag{23}$$

If the external restraint force is larger than the cracking load, $N_{cr} = f_{ctm}A_{I,eff}$, a new crack will form and the calculation using Eqs. (20)–(21) is repeated with $n_{cr} = 2$. This iterative process of successively increasing the number of cracks is continued until the external restraint force is lower than the cracking load, which implies that no new cracks will form. For more information about the external restraint force model, see Refs. [36,37].

5. Results

In this chapter, the results from the developed models are shown. In Section 5.1, the results from the optimisation based on the European standard 16432-2 [2] is presented. The obtained optimised dimensions are then applied in the dynamic vehicle–track interaction model, see Section 5.2, and the model of reinforced concrete, see Section 5.3.

5.1. European standard

Based on the optimisation problem described in Section 2.2, a design was developed that minimises the amount of CO_2 emissions from the concrete in the construction of slab track. The optimisation problem was solved in Matlab using the non-linear programming solver *fmincon*. The results from the optimisation are shown in Table 5. From a sensitivity analysis, it has been verified that similar optimised dimensions are obtained for rail pad stiffnesses spanning from 25 kN/mm to 40 kN/mm. From the optimisation, it can be seen that the widths of both the panel and roadbed have converged to the specified lower bounds. Further, as expected, it is seen that the thicknesses of the concrete layers tend to be smaller for the high-performing concrete (in particular the thickness of the roadbed). However, the low-quality concrete (C25/30) produces the lowest amount of CO_2 emissions since less cement is required per cubic metre compared to the other types of concrete. The variation in emission between the different concrete types is, however, not very significant.

In order to pass the standard, there is a trade-off between having a thinner panel or a thinner roadbed. For a specific type of concrete, the optimised dimensions are dependent on how the influences of the two cross-sections are weighted in the objective function, see Eq. (1). In this study, the weighting was obtained based on the amount of cement per unit volume for each layer. In Fig. 6, the results from a parametric study are shown where the upper-right area corresponds to thickness combinations of the concrete layers that would pass the standard, while the lower-left area represents combinations that would not pass. In addition, the calculated optimised design is indicated. In the parametric study, the lower bound for each width, which the optimisation problem converged to, has been used. From Fig. 6, it is seen that the lines have discontinuous derivatives at certain thicknesses. These discontinuous derivatives occur since the limiting safety factor for the design is changed at these thicknesses.

In this paper, the focus is on the design of a slab track considering the dynamic effects induced by a passing passenger vehicle and most of the simulations were therefore conducted using an axle load of 17 tonnes, see Fig. 6(a). However, it is also important to consider the effects of occasional traffic with higher axle loads, e.g. a maintenance vehicle. For comparison, Fig. 6(b) illustrates the trade-off between panel and roadbed thicknesses when accounting for a higher axle load. In both Fig. 6(a) and (b), it can be seen that the trade-off is smaller when the quality of the concrete in the panel is increased. Finally, since there is much more cement per unit volume in the panel compared to the roadbed, the optimal solution has converged to a situation where the panel thickness is close to the minimum value that would pass the standard.

To further investigate the effect of a different axle load, additional parametric studies were conducted where the optimised dimensions were evaluated for axle loads spanning from 15 to 30 tonnes. The results for all considered concrete types in the panel are shown in Fig. 7. It is seen that the thickness of the concrete panel is close to being constant, while there is a significant variation in the thickness of the roadbed. As discussed earlier, this result occurs since there is more cement in the panel which implies that the solution strives towards a panel thickness that is close to the minimal value required in the standard. Hence, similar panel thicknesses were found for all considered concrete qualities, and the optimum way to design for increased axle loads is to increase the thickness of the roadbed. Furthermore, it can be seen that although the thicknesses are increased when using C25/30 for the panels, this type of concrete still results in the lowest CO_2 emissions since less cement is used per unit volume.

5.2. Dynamic vehicle–track interaction model

The dynamic performance of the optimised slab track designs from Section 5.1 has been assessed using simulations with either uncracked or cracked sections of the concrete panel. Furthermore, the influence of the panel thickness on the maximum principal stress in the panel has been analysed. To limit the number of investigations, only the C25/30 concrete type is considered in this section since this type of

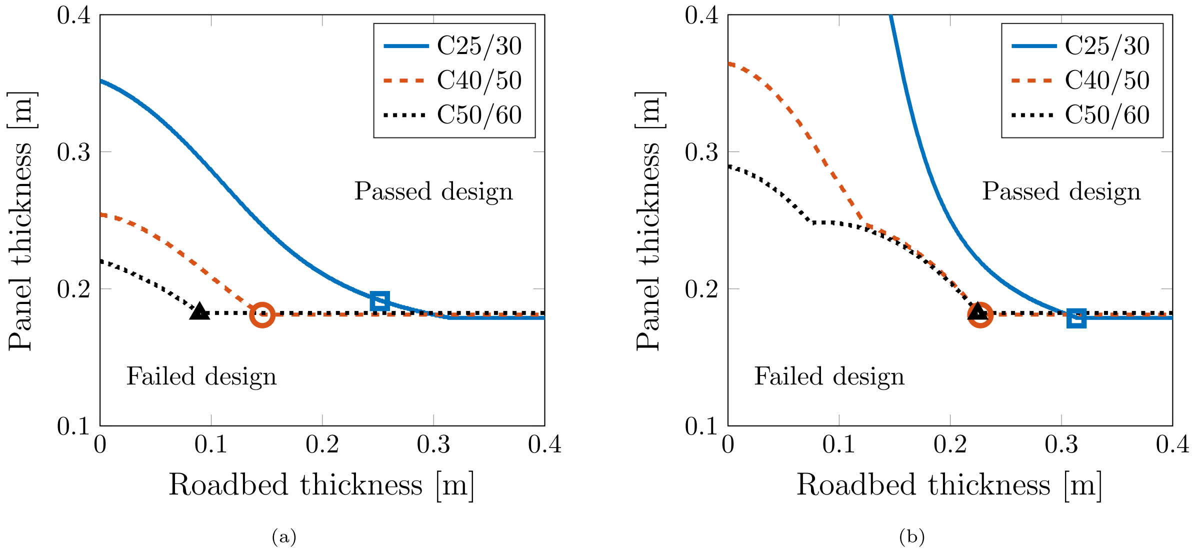

Fig. 6. Combinations of panel and roadbed thicknesses that would pass or fail the European standard 16432-2 [2] for each type of concrete when using axle load (a) 17 tonnes and (b) 25 tonnes. The markers in the figure indicate the optimised dimensions.

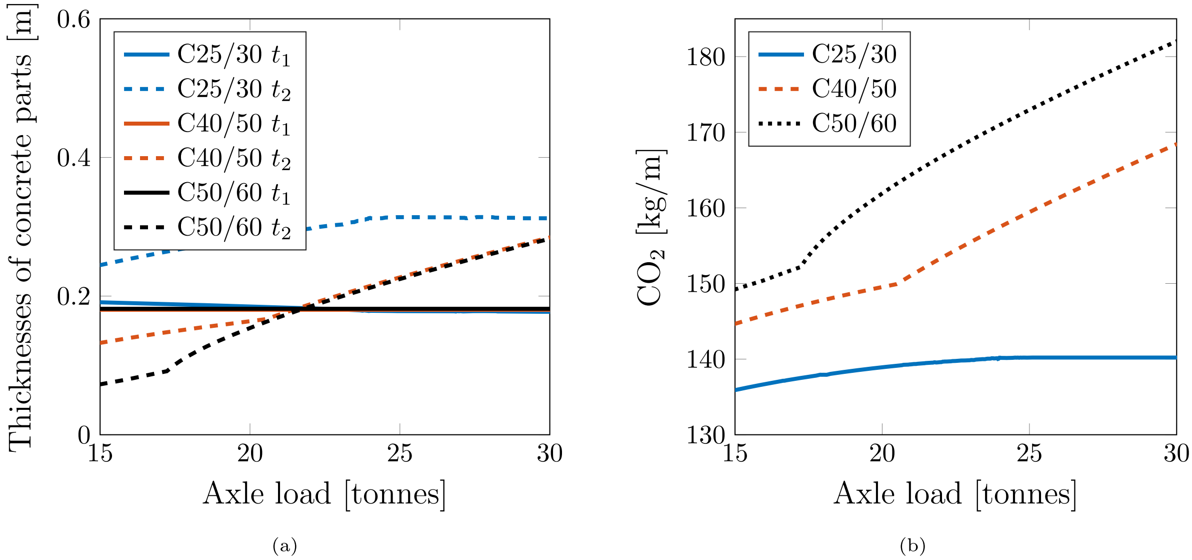

Fig. 7. (a) Optimal thicknesses of the concrete parts as a function of axle load. Note that it is only in the panel where the type of concrete has been changed. For the roadbed, the same concrete type was used in all simulations. The thicknesses t_1 and t_2 are defined in Fig. 2. (b) Resulting CO_2 emissions per metre built track.

concrete resulted in the lowest CO_2 emissions in the optimisation, see Section 5.1.

When considering the dynamic vehicle–track interaction, the level of irregularities in vertical track geometry (longitudinal level) will affect the track response significantly. One particularly severe type of track irregularity is rail corrugation, which has been studied in detail by e.g. Correa et al. [38]. Track irregularities can, according to the European standard 13848-6 [39], be divided into different track classes depending on the standard deviation of the irregularity (ranging from A to E). In this paper, realisations (samples) of track irregularities, as a function of longitudinal track position, were calculated based on a Power Spectral Density (PSD) function according to Claus and Schiehlen [40]. For each realisation, different (uncorrelated) track irregularities were considered for the two rails, which induced a non-symmetric excitation. The irregularities were generated by a summation of sine functions with amplitudes according to the PSD and random phase angles for wavelengths in the interval 1–25 m. The samples were then scaled such that the standard deviation of the irregularities in longitudinal level corresponded to the limit value for each track class described in Ref. [39]. At vehicle speed 250 km/h, the studied wavelength interval corresponds to dynamic excitations in the frequency range 3–69 Hz. The fundamental resonance of the coupled vehicle–track system, which may significantly influence the dynamic response of the track [17], can generally be found within this frequency range.

In Fig. 8, the calculated maximum wheel–rail contact force, normalised with the static wheel load, is shown for the different track classes. For each track class, five realisations were generated from the PSD and in Fig. 8, the mean values are shown. The simulations were conducted for three different panel conditions: (i) uncracked panel section (ii) cracked panel section without long-term effects and (iii) cracked panel section including long-term effects. The influence of a cracked section was modelled by reducing the bending stiffness based on the results from the reinforced concrete model (RCM), see Sections 4 and 5.3. When considering a cracked section and no long-term effects, the elastic modulus of the concrete was not changed, whereas the panel thickness was reduced in Abaqus such that the same bending stiffness was obtained as in the RCM. When long-term effects were accounted

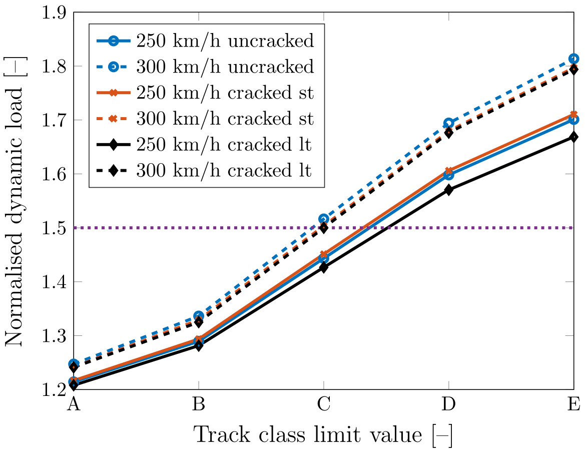

Fig. 8. Ratio between the maximum dynamic wheel–rail contact force and the static load for different track classes, vehicle speeds and concrete panel conditions. The abbreviations 'st' and 'lt' stand for short-term and long-term. Optimised dimensions from Section 5.1 and concrete class C25/30. The horizontal line indicates the dynamic amplification factor used in the European standard 16432-2 [2].

Table 6
Normalised standard deviation of maximum wheel–rail contact force at vehicle speed 250 km/h.

	Uncracked	Cracked short term	Cracked long term
Track class A	0.027	0.026	0.028
Track class B	0.035	0.034	0.036
Track class C	0.050	0.049	0.051
Track class D	0.062	0.059	0.062
Track class E	0.069	0.067	0.069

for, the elastic modulus of the concrete was reduced in Abaqus to the effective value predicted by the RCM, while the panel thickness was set to a value such that the bending stiffness was the same for both models.

From Fig. 8, it can be seen that the influence of a cracked panel section on the maximum wheel–rail contact force is small. However, changing the vehicle speed or track class would change the maximum value of the wheel–rail contact force significantly. It is observed that the dynamic amplification factor 1.5 prescribed in the European standard 16432-2 [2] is conservative as long as the track quality can be maintained to qualify for track class A or B.

The standard deviation of the calculated maximum wheel–rail contact force between the different realisations, normalised with the mean value, are shown in Tables 6 and 7. From the tables, it can be seen that there is a trend towards a larger spread in maximum wheel–rail contact force when considering more severe track irregularities. As for the mean values, it is seen that similar standard deviations were obtained for both cracked and uncracked sections. Further, it is noticed that the standard deviations were slightly higher for the lower speed. The reason for this is that one realisation of track irregularity when running at 250 km/h resulted in a slightly higher maximum wheel–rail contact force compared to when the other realisations were considered. This effect was not as significant for the higher speed. Since only the magnitude of the irregularity was changed between the different track classes, the same trend is seen for all classes. Finally, it should be noticed that even though there are some differences in the standard deviations when considering different track classes and speeds, it should be emphasised that the spread between the realisations is small.

It is expected that the requirements on the quality and maintenance level of track would vary depending on what type of traffic is considered. For example, when considering a slab track built for high-speed applications, it is not realistic to allow track class E. For such a high-performance track, strict requirements would be used. In the following simulations, track class C was used and considered as a worst-case scenario. In addition, a vehicle speed of 250 km/h has been studied exclusively.

Table 7
Normalised standard deviation of maximum wheel–rail contact force at vehicle speed 300 km/h.

	Uncracked	Cracked short term	Cracked long term
Track class A	0.020	0.016	0.021
Track class B	0.028	0.022	0.028
Track class C	0.037	0.030	0.040
Track class D	0.045	0.038	0.048
Track class E	0.050	0.041	0.054

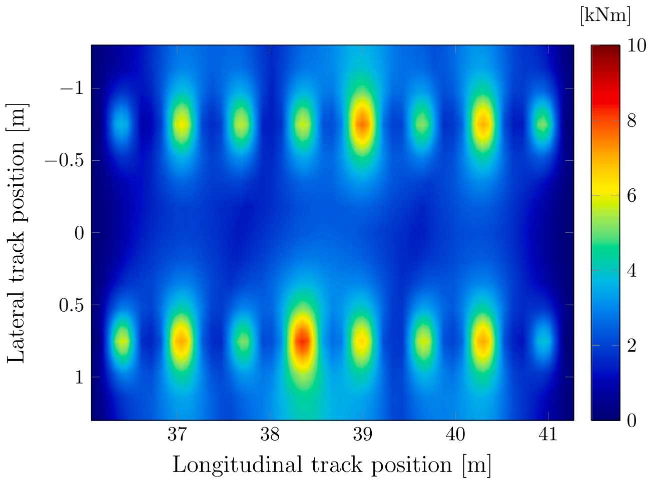

Fig. 9. Distribution of maximum bending moment that causes stress in the longitudinal direction in the concrete panel (maximum value 8.54 kNm). Vehicle speed 250 km/h, uncracked section, track class C, concrete class C25/30 and optimised dimensions from Section 5.1.

The maximum bending moment for a certain concrete type and state was calculated using the dynamic vehicle–track interaction model. Based on the time history of the wheel–rail contact forces, a post-processing simulation has been conducted in Abaqus. From this simulation, the time history of the spatially varying bending moment was calculated. For one realisation of track irregularities, Figs. 9 and 10 show the distributions of maximum (evaluated over the complete simulated time history) bending moment in the longitudinal and lateral directions for an uncracked section. From the figures, it is observed that the bending moment is higher below the rail seats. Furthermore, it can be seen that the maximum bending moment occurs in the lateral direction. Note that the magnitude of the bending moment is different at the different rail seats since different track irregularity profiles generated using the PSD were used for the two rails inducing irregularities in both longitudinal level and twist.

The maximum principal stress in the concrete panel is another important response to consider in the optimisation of slab track. In Fig. 11, again for one realisation of track irregularities, the maximum principal stress is shown as a function of spatial position. Similar to the distribution of bending moment, it can be seen that stress concentrations occur at each rail seat. To determine if the panel will crack or not, the maximum principal stress can be compared with the mean flexural tensile strength. According to Eurocode 2 [22], the mean flexural tensile strength can be determined as

$$f_{\mathrm{ctm,fl}} = \max\Big((1.6 - t_1) f_{\mathrm{ctm}},\ f_{\mathrm{ctm}}\Big), \tag{24}$$

where t_1 is given in metres. When implementing the optimised slab track design for C25/30 from Section 5.1, the mean flexural tensile strength becomes $f_{\mathrm{ctm,fl}} = 3.67$ MPa, which is significantly higher than the maximum principal stress of 1.63 MPa calculated with the dynamic model, cf. Fig. 11. This implies that the stress levels in the panel, due

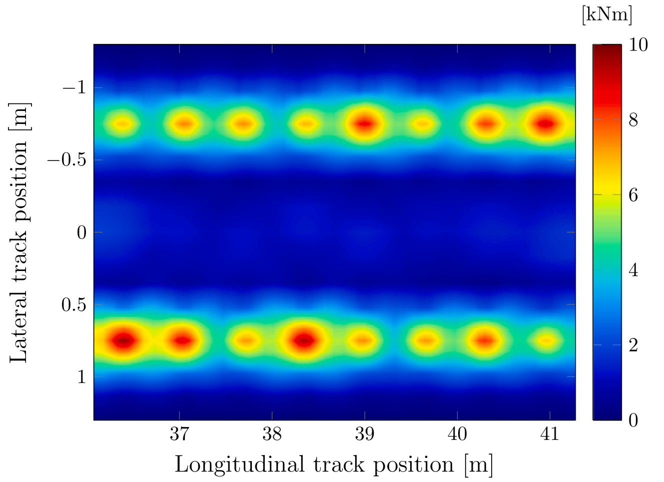

Fig. 10. Distribution of maximum bending moment that causes stress in the lateral direction in the concrete panel (maximum value 9.72 kNm). Vehicle speed 250 km/h, uncracked section, track class C, concrete class C25/30 and optimised dimensions from Section 5.1.

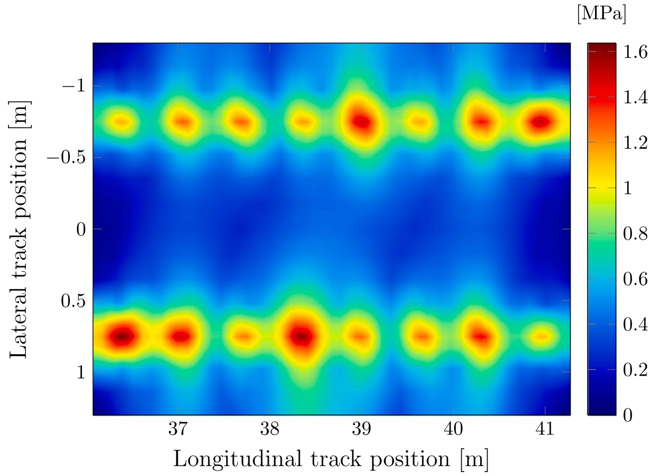

Fig. 11. Distribution of maximum principal stress in the concrete panel (maximum value 1.63 MPa). Vehicle speed 250 km/h, uncracked section, track class C, concrete class C25/30 and optimised dimensions from Section 5.1.

Table 8
Normalised standard deviation.

Maximum bending moment lateral direction	Maximum bending moment longitudinal direction	Maximum principal stress
0.072	0.059	0.071

to the load from the vehicle, will not cause cracking and there may be a potential to reduce the thickness.

The results presented in Figs. 9–11 were obtained from one sample of track irregularities. In order to investigate the spread in maximum bending moment and maximum principal stress between different realisations of track irregularities, these properties were calculated for five different realisations (similar to the maximum wheel–rail contact force). In Table 8, the normalised standard deviation is shown for each response. From the table, it is observed that the spread between the different realisations is similar to the spread in maximum wheel–rail contact force.

For a given sample of track irregularity, the maximum principal stress as a function of panel thickness is shown in Fig. 12. The variation of maximum principal stress is shown for three different bed moduli,

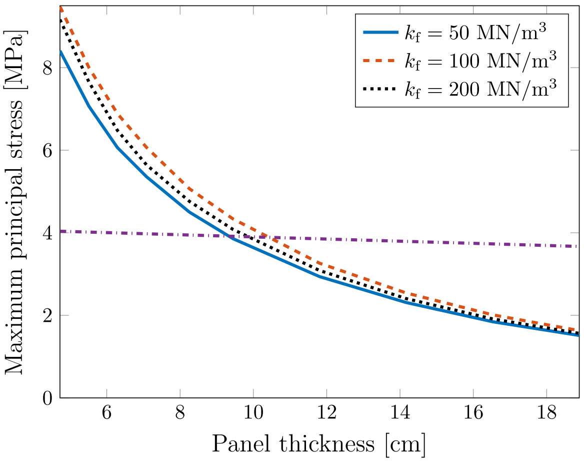

Fig. 12. Maximum principal stress in the concrete panel as a function of panel thickness for three different soil stiffnesses (bed moduli). Vehicle speed 250 km/h, uncracked section, track class C, concrete class C25/30 and optimised roadbed thickness from Section 5.1. The straight line indicates the mean flexural tensile strength, which is also influenced by panel thickness.

and it can be seen that the influence of the soil stiffness is small. To understand why, recall that it can be shown that the maximum bending moment and maximum stress are proportional to $k_\mathrm{f}^{-1/4}$ when considering a beam on an elastic foundation model [41]. However, in agreement with previous studies, cf. Ref. [42], it was found that the magnitudes of the vertical wheel–rail contact forces were generally higher for a higher foundation stiffness. Thus, the combined influence from these effects was that the impact of soil stiffness value on the maximum principal stress in the concrete panel was limited.

To determine the minimum thickness of the concrete panel without risk for cracking due to the dynamic load from the vehicle, also the mean flexural tensile strength is shown in Fig. 12. By comparing the maximum principal stress with the mean flexural tensile strength, it can be seen that the panel would crack if the thickness was smaller than or equal to 10 cm. This thickness is significantly smaller than the optimised thickness of 19 cm calculated with the European standard 16432-2 [2], cf. Table 5. When evaluating these results from the dynamic model, it should be emphasised that the stress levels would increase if other irregularities were added besides the irregularities in longitudinal level. As an example, wheel tread irregularities inducing an excitation at higher frequencies than considered here (out-of-round wheels, wheel flats, etc.) and irregularities in soil stiffness (along and across the roadbed, differential settlement, washouts, etc.) may increase the wheel–rail contact forces and the maximum principal stress. In addition, when soil stiffness irregularities are present, the static stress contribution from the dead weight of the panel may not be negligible. Furthermore, since the influence of external restraint forces is neglected in the dynamic model, additional calculations are required if it cannot be proven that the level of external restraint is small. Accounting for external restraint in the dynamic model and irregularities in the soil and vehicle are, however, outside of the scope of this paper.

5.3. Model of reinforced concrete

By applying the model of reinforced concrete, the bending stiffness of a cracked panel section has been determined and crack widths have been estimated. All three types of concrete defined in Section 2.2 have been analysed. In Table 9, the resulting bending stiffnesses per metre are shown when a concrete cover thickness of c = 20 mm is used. As expected, the bending stiffness is higher in State I (uncracked) compared to State II (cracked). The bending stiffness is reduced even further when taking long-term effects into account. The optimised dimensions

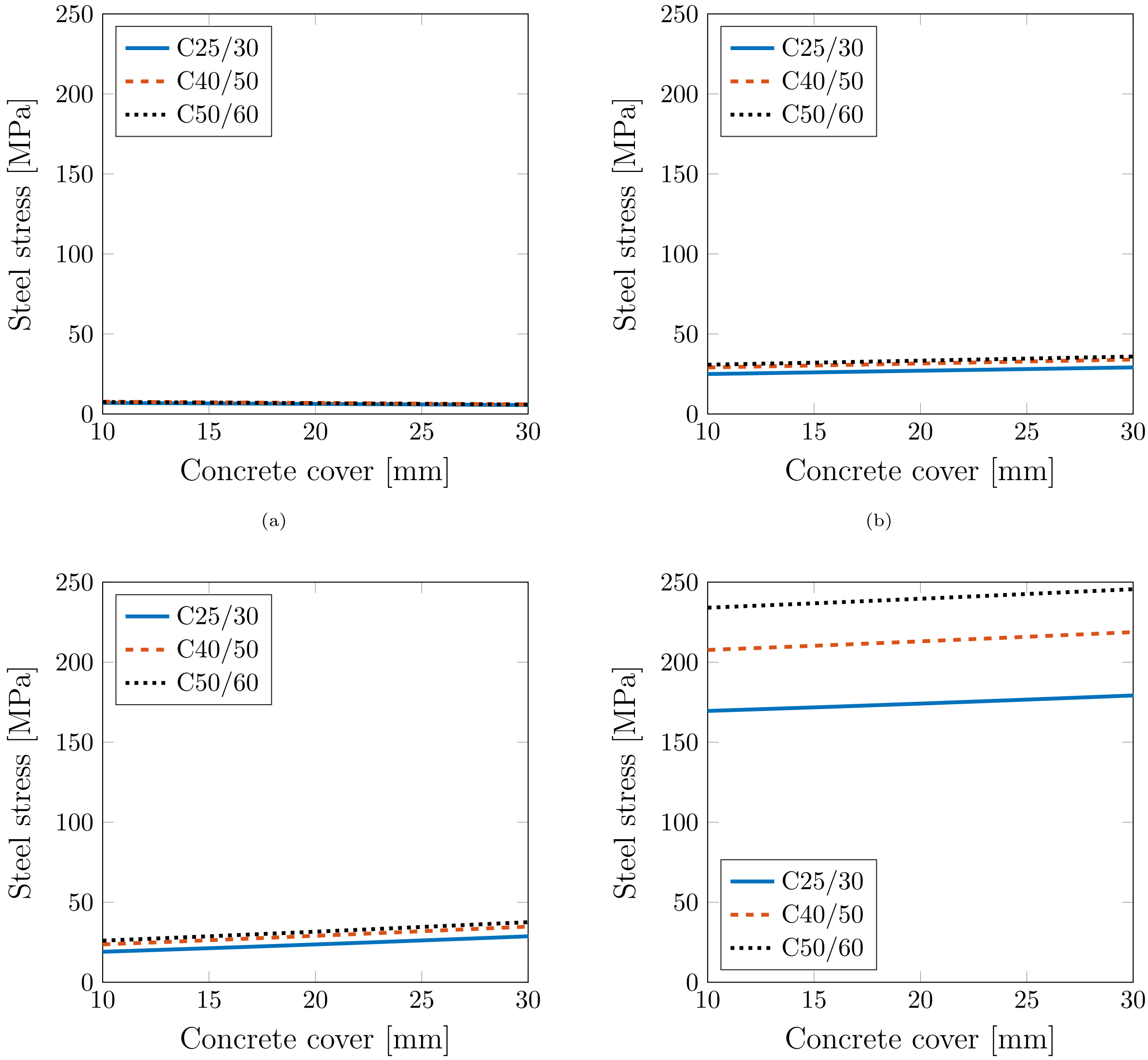

(a) (b) (c) (d)

Fig. 13. Maximum steel stress as a function of the thickness of the concrete cover for (a) State I short-term and no restraint, (b) State II short-term and no restraint, (c) State II long-term and no restraint and (d) State II long-term and full restraint. Vehicle speed 250 km/h and track irregularity class C.

Table 9
Bending stiffness per metre for cracked and uncracked sections when using the optimised solutions presented in Table 5.

	EI_{I} [MNm]	$EI_{\mathrm{II,st}}$ [MNm]	$EI_{\mathrm{II,lt}}$ [MNm]
C25/30	20.8	7.0 (33.9%)	5.7 (27.4%)
C40/50	19.9	6.3 (31.8%)	5.3 (26.6%)
C50/60	21.4	6.6 (30.7%)	5.6 (26.1%)

according to the results in Section 5.1 were used giving different panel thicknesses for the different concrete types. When comparing the results between different concrete types, it was found that the moment of inertia was decreased with increasing concrete quality due to the smaller thicknesses and smaller effective modular ratios. Thus, since the elastic modulus is increased with increasing concrete quality, the bending stiffness becomes rather similar for all types of concrete.

Similarities and differences between concrete types and states have been assessed by calculating the steel stresses. To this end, the bending moment was determined by using the dynamic vehicle–track interaction model, see Sections 3 and 5.2. As described in Section 5.2, when the bending moment of a cracked section was calculated, the thickness and elastic modulus of the concrete panel in the dynamic model were calibrated such that the same bending stiffness was used for both models.

In Fig. 13, the calculated maximum value of the steel stress is shown as a function of the thickness of the concrete cover. The main purpose of the concrete cover is to reduce the risk of corrosion of the reinforcement, and its thickness may vary between different applications and designs. When the stresses were calculated, the track irregularity class C was applied (see Section 5.2 for more information). As expected, the maximum steel stresses are lower in State I compared to State II and the highest steel stress occurs when both long-term effects and full external restraint are considered. The magnitude of the maximum steel stress is, however, always lower than the yield stress (f_{ys} = 500 MPa). By comparing the stress levels with either no or full external restraint, it is seen that the influence of the external restraint is very significant. In practice, the stress levels of a cracked section will be somewhere between the solutions assuming no or full external restraint. In addition, it is noted that the difference in the maximum steel stress between the different concrete types is small. From additional simulations conducted using the dynamic vehicle–track interaction model (not presented here), it has been verified that the influence of the thickness

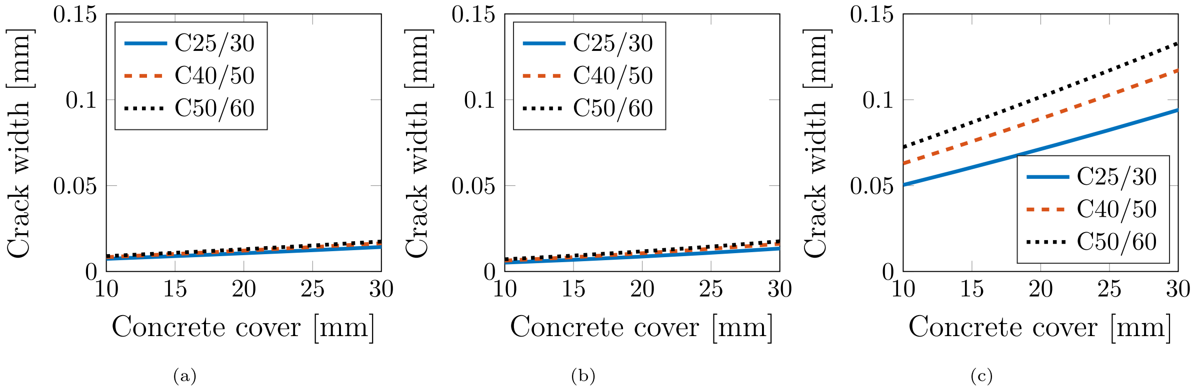

(a) (b) (c)

Fig. 14. Crack width as a function of the thickness of the concrete cover considering (a) short-term response and no restraint, (b) long-term response and no restraint and (c) long-term response and full restraint. Vehicle speed 250 km/h and track irregularity class C.

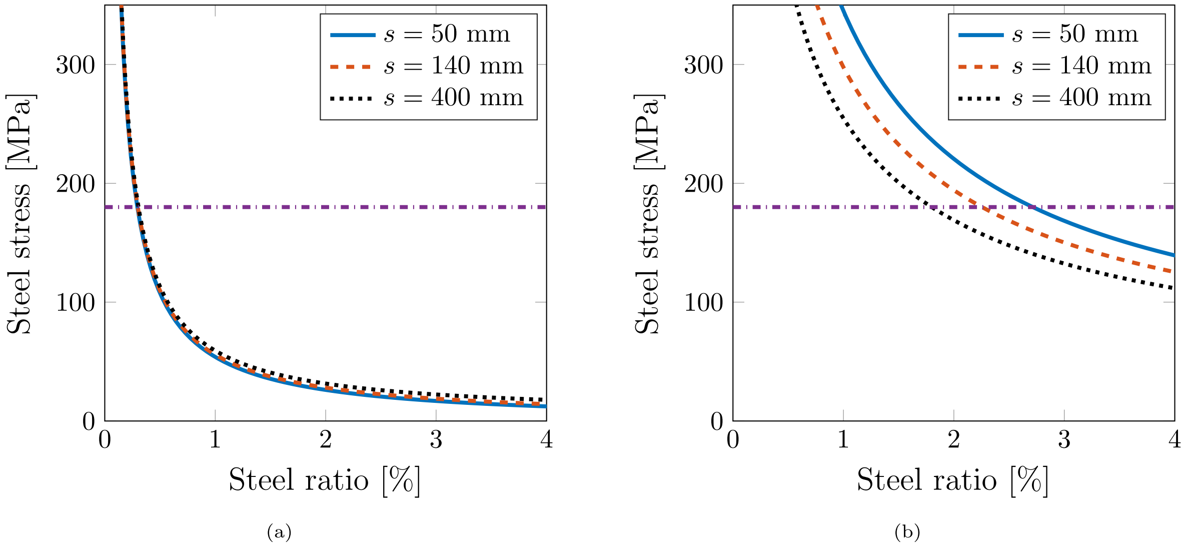

(a) (b)

Fig. 15. Steel stress as a function of steel ratio for different reinforcement spacings assuming (a) no restraint and (b) full restraint. The horizontal lines indicate the limit value when the equivalent stress is equal to the reduced fatigue limit.

of the concrete cover on the magnitude of the bending moment is small. Therefore, the bending moment calculated for $c = 20$ mm was used when the stresses were evaluated. Exploiting the fact that the same bending moment can be used for a range of different concrete covers drastically reduced the computational cost.

Interestingly, it can be seen that the steel stress is decreased with increasing thickness of the concrete cover in State I, but increased with increasing concrete cover in State II. To understand why, recall that two properties that affect the magnitude of the steel stress are the moment of inertia and the distance from the neutral axis to the reinforcement bars in tension. When the thickness of the concrete cover is increased for a given section thickness, both the moment of inertia and the distance from the neutral axis to the reinforcement bar are decreased. However, in State I, the ratio between the moment of inertia and the distance is increasing with increasing thickness of the concrete cover. On the other hand, in State II, the same ratio is decreasing with increasing thickness of the concrete cover. This difference between the states occurs since the relative change in the moment of inertia as a function of concrete cover is greater when the section is cracked.

Also the crack widths were estimated using the theory outlined in Section 4. In Fig. 14, the crack width as a function of the thickness of the concrete cover is shown for (a) short-term response and no external restraint, (b) long-term response and no external restraint and (c) long-term response and full external restraint. From the figure, it is seen that the crack width is increasing with increasing thickness of the concrete cover. The crack width can be compared with the crack width limit. According to the European standard 16432-2 [2], Eurocode 2 [22] shall be used to determine the crack width limit for prefabricated slabs, which results in a crack width limit of 0.3 mm for the panel. From the figure, it is seen that the crack width is below the crack width limit for all considered thicknesses of concrete cover.

Since both the steel stress and crack width are below the yield limit and crack width limit, there is a possibility to reduce the amount of steel reinforcement and by that reduce the environmental impact from slab track even further. The amount of steel reinforcement can be reduced by either using fewer bars and/or thinner bars. In Fig. 15, the calculated steel stress when using the concrete class C25/30 is shown as a function of steel ratio for three different reinforcement spacings. The steel ratio is defined as the cross-sectional area of the reinforcement divided by the total cross-sectional area of the slab. The calculation was performed when taking long-term effects into account and assuming (a) no external restraint and (b) full external restraint. The stress levels are compared with a limit value where the equivalent stress is equal to the reduced fatigue limit. The equivalent stress was calculated assuming a pulsating loading and a Smith–Watson–Topper mid-stress correction, whereas the reduced fatigue limit was determined assuming that the nominal fatigue limit is half of the ultimate tensile strength and that the total reduction factor is 0.85. From Fig. 15, it is observed that the stress levels are significantly lower when assuming no external restraint. This implies that the amount of steel reinforcement in the slab track design

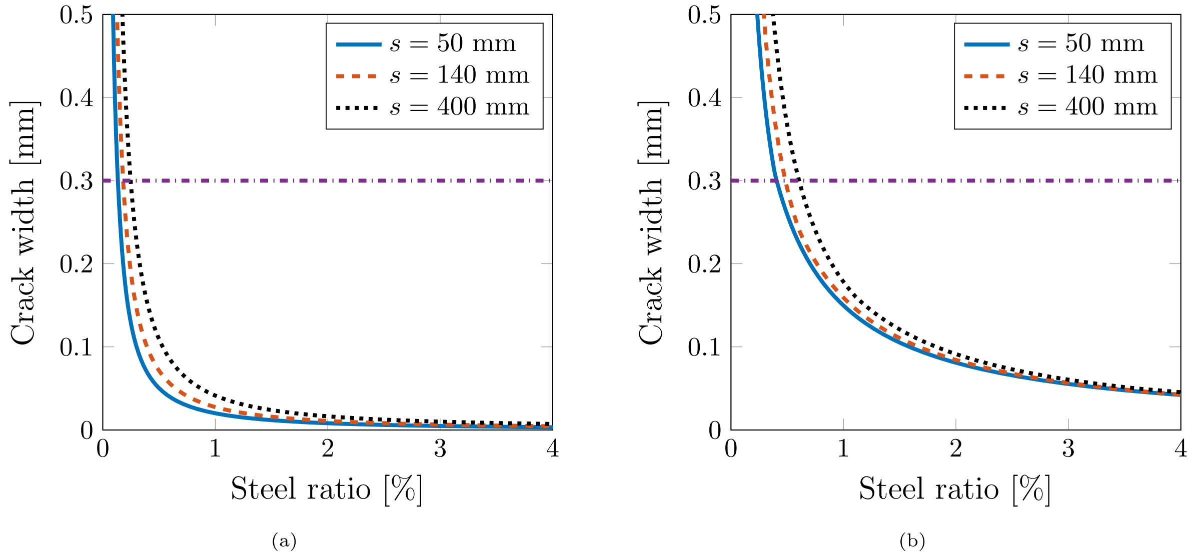

Fig. 16. Crack width as a function of steel ratio for different reinforcement spacings assuming (a) no restraint and (b) full restraint. The horizontal lines indicate the crack width limit.

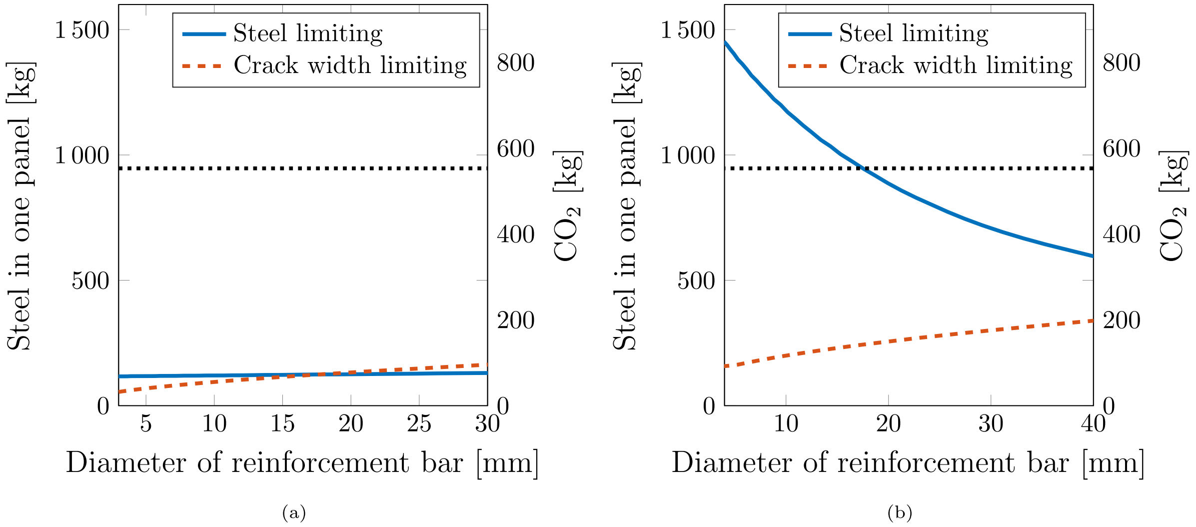

Fig. 17. Amount of steel and corresponding CO_2 emission from one concrete panel just fulfilling the requirement related to steel stress or crack width when assuming (a) no restraint and (b) full restraint. The horizontal lines indicate the amount of steel and CO_2 emission level when s = 140 mm and ϕ = 20 mm.

can be reduced substantially if it can be proven that the design has no (or little) external restraint. In Fig. 16, predicted crack widths are compared to the limit value 0.3 mm given in Ref. [28]. Similar to Fig. 15, it can be seen that the external restraint has a significant effect.

In Fig. 17, the minimum amount of steel in one concrete panel is shown as a function of the diameter of the reinforcement bars. The minimisation was conducted by calculating the maximum reinforcement spacing that can be used while still fulfilling the requirements, i.e. the equivalent stress is below the reduced fatigue limit, and the maximum crack width is below the crack width limit. Note that when using the minimum amount of steel, also the reinforcement spacing is varying with the bar diameter. When the amount of steel was calculated, a steel density of ρ_s = 7800 kg/m^3 was used and the same dimensions were assumed for the reinforcement bars in the lateral and longitudinal directions and in the upper and lower reinforcement layers. Further, also the CO_2 emission from the steel within one panel is presented in the figure. The CO_2 emission related to the steel was calculated using the scaling factor $\alpha_s = 0.548$ [43].

The minimised amount of steel in the optimised reinforcement configurations has been compared with the amount of steel when using the parameter values in the calculation example in the European standard 16432-2 [2]: s = 140 mm and ϕ = 20 mm. From Fig. 17, it is seen that the steel stress is limiting in most configurations and that much less steel is required when assuming no external restraint.

6. Conclusions

The static calculation method presented in the European standard 16432-2 [2] has been implemented and used to optimise a slab track design. The objective of the optimisation was to minimise the environmental impact from the concrete parts while still fulfilling the requirements of the standard. In the optimisation, thicknesses and widths of the rectangular concrete panel and roadbed, and three different qualities of concrete were considered. From the optimisation, a trade-off between the thicknesses of the concrete parts could be seen, where a thinner panel was prioritised since more cement per unit volume is used here as compared to the roadbed.

The optimised dimensions were used as input to a 3D model of dynamic vehicle–track interaction. From the dynamic simulations, it was concluded that the level of vertical track irregularities and vehicle speed had a significant effect on the maximum wheel–rail contact force, while the corresponding influence of cracks in the concrete panel was negligible. When the maximum principal stress in the concrete panel was calculated, it was concluded that the panel thickness can be reduced even further without the risk of crack initiation if the degree of external restraint is low. Reducing the thickness of the concrete panel can lower the environmental impact from slab track significantly. For the given traffic scenario studied in this paper, a thickness reduction from 19 cm (optimised thickness based on the requirements in the calculation method in the EN standard for C25/30) to 10 cm (thickness that resulted in crack initiation due to the dynamic vehicle load, see Fig. 12) would reduce the CO_2 emission from the concrete parts by 35%.

The maximum bending moment, obtained from the dynamic model, was used as input to a model of reinforced concrete to calculate the stress in the reinforcement and resulting crack widths for different reinforcement configurations. The model of reinforced concrete was also used to calculate the bending stiffness of a cracked concrete section, which was used as an updated input parameter for the dynamic model. From the reinforced concrete model, it was concluded that the external restraint degree has a significant effect on the steel stresses and crack widths. In particular, it was noted that the amount of reinforcement can be reduced significantly compared to the dimensions presented in the calculation example in the European standard 16432-2 [2] if it can be proven that the degree of external restraint is low.

In a calculation of the distributions of maximum principal stress and maximum bending moment, it was found that the responses were significant only below the rail seats. This opens up for future work, where the environmental impact of slab tracks can be reduced even further by a geometry optimisation that excludes much of the concrete between the rails, e.g. by adopting a ladder-like structure. Other examples of possible future extensions include studies of the effect of varying stiffness in the panel, i.e. cracked in some parts and uncracked in other parts, and estimations of external restraint degrees in slab tracks and measures to reduce these external restraints. Finally, it should be noted that the bed moduli used in this paper have been taken as uniform and constant in the longitudinal and lateral directions.

CRediT authorship contribution statement

Emil Aggestam: Conceptualization, Methodology, Software, Writing – original draft, Writing – review & editing, Visualization. **Jens C.O. Nielsen:** Conceptualization, Methodology, Supervision, Proofreading. **Karin Lundgren:** Conceptualization, Methodology, Supervision, Proofreading. **Kamyab Zandi:** Conceptualization, Methodology, Supervision. **Anders Ekberg:** Conceptualization, Methodology, Supervision, Proofreading.

Declaration of competing interest

The authors declare that they have no known competing financial interests or personal relationships that could have appeared to influence the work reported in this paper.

Acknowledgements

The current study is part of the on-going activities within CHARMEC — Chalmers Railway Mechanics (www.chalmers.se/charmec). Parts of the study have been funded from the European Union's Horizon 2020 research and innovation programme in the projects In2Track2 and In2Track3 under grant agreements Nos 826255 and 101012456. In particular, the support from Trafikverket (the Swedish Transport Administration) and Abetong AB are acknowledged. Discussions with Dr Rikard Bolmsvik, Abetong AB, and Drs Andreas Andersson and Martin Li, Trafikverket, are gratefully acknowledged. Parts of the simulations were performed using resources at Chalmers Centre for Computational Science and Engineering (C3SE) provided by the Swedish National Infrastructure for Computing (SNIC).

References

[1] Zandi K, Lundgren K, Lövgren I. Ballastless track – Minimizing the climate impact. Tech. rep., Gothenburg, Sweden: Department of Architecture and Civil Engineering, Chalmers University of Technology; 2021, p. 1–50.

[2] EN 16432-2 CEN Standard. Railway applications – Ballastless track systems – Part 2: System design, subsystems and components. 2017.

[3] Knothe K, Grassie S. Modelling of railway track and vehicle/track interaction at high frequencies. Veh Syst Dyn 1993;22(3–4):209–62.

[4] Connolly D, Kouroussis G, Laghrouche O, Ho C, Forde M. Benchmarking railway vibrations – Track, vehicle, ground and building effects. Constr Build Mater 2015;92:64–81.

[5] Nielsen JCO, Igeland A. Vertical dynamic interaction between train and track – Influence of wheel and track imperfections. J Sound Vib 1995;187(5):825–39.

[6] Zhai W, Sun X. A detailed model for investigating vertical interaction between railway vehicle and track. Veh Syst Dyn 1994;23(S1):603–15.

[7] Ripke B, Knothe K. Simulation of high frequency vehicle-track interactions. Veh Syst Dyn 1995;24:72–85.

[8] Zhai W, Wang K, Cai C. Fundamentals of vehicle–track coupled dynamics. Veh Syst Dyn 2009;47(11):1349–76.

[9] Sadeghi J, Khajehdezfuly A, Esmaeili M, Poorveis D. Investigation of rail irregularity effects on wheel/rail dynamic force in slab track: Comparison of two and three dimensional models. J Sound Vib 2016;374:228–44.

[10] Theyssen JS, Aggestam E, Zhu S, Nielsen JCO, Pieringer A, Kropp W, Zhai W. Calibration and validation of the dynamic response of two slab track models using data from a full-scale test rig. Eng Struct 2021;234:111980.

[11] Zhai W, Xia H, Cai C, Gao M, Li X, Guo X, Zhang N, Wang K. High-speed train–track–bridge dynamic interactions – Part I: Theoretical model and numerical simulation. Int J Rail Transp 2013;1(1–2):3–24.

[12] Zhai W, Wang S, Zhang N, Gao M, Xia H, Cai C, Zhao C. High-speed train–track–bridge dynamic interactions – Part II: Experimental validation and engineering application. Int J Rail Transp 2013;1(1–2):25–41.

[13] Luo J, Zhu S, Zhai W. Development of a track dynamics model using Mindlin plate theory and its application to coupled vehicle-floating slab track systems. Mech Syst Signal Process 2020;140:106641.

[14] Yang J, Zhu S, Zhai W. A novel dynamics model for railway ballastless track with medium-thick slabs. Appl Math Model 2020;78:907–31.

[15] Nielsen JCO, Li X. Railway track geometry degradation due to differential settlement of ballast/subgrade – Numerical prediction by an iterative procedure. J Sound Vib 2018;412:441–56.

[16] Aggestam E, Nielsen JCO. Multi-objective optimisation of transition zones between slab track and ballasted track using a genetic algorithm. J Sound Vib 2019;446:91–112.

[17] Aggestam E, Nielsen JCO. Simulation of vertical dynamic vehicle–track interaction using a three-dimensional slab track model. Eng Struct 2020;222:110972.

[18] Poveda E, Rena CY, Lancha JC, Ruiz G. A numerical study on the fatigue life design of concrete slabs for railway tracks. Eng Struct 2015;100:455–67.

[19] Zhu S, Cai C. Stress intensity factors evaluation for through-transverse crack in slab track system under vehicle dynamic load. Eng Fail Anal 2014;46:219–37.

[20] Milford RL, Allwood JM. Assessing the CO2 impact of current and future rail track in the UK. Transp Res D: Transp Environ 2010;15(2):61–72.

[21] Hahrs F, Malmberg J, Mohlén M. Dimensioning of slabs for high-speed railway lines. (Bachelor's thesis), Kalmar and Växjö, Sweden: Faculty of Technology, Linnaeus University; 2016, p. 1–53.

[22] EN 1992-1-1 CEN Standard. Eurocode 2: Design of concrete structures – Part 1-1: General rules and rules for building. 2004.

[23] Rahrovani S. Structural reliability and identification with stochastic simulation (Ph.D. thesis), Gothenburg, Sweden: Department of Applied Mechanics, Chalmers University of Technology; 2016.

[24] Tarifa M, Zhang X, Ruiz G, Poveda E. Full-scale fatigue tests of precast reinforced concrete slabs for railway tracks. Eng Struct 2015;100:610–21.

[25] Rezaie F, Shiri M, Farnam S. Experimental and numerical studies of longitudinal crack control for pre-stressed concrete sleepers. Eng Fail Anal 2012;26:21–30.

[26] Zi G, Lee S-J, Jang SY, Yang SC, Kim S-S, et al. Investigation of a concrete railway sleeper failed by ice expansion. Eng Fail Anal 2012;26:151–63.

[27] You R, Li D, Ngamkhanong C, Janeliukstis R, Kaewunruen S. Fatigue life assessment method for prestressed concrete sleepers. Front Built Environ 2017;3:68.

[28] EN 1992-1-1 CEN Standard. Eurocode 2: Design of concrete structures – Concrete bridges – Design and detailing rules. 2005.

[29] Cementa AB HG. Environmental product declaration (EPD) portland fly ash cement CEM II/A-V 42.5 n. 2016.

[30] Abaqus. Abaqus documentation. Providence, RI, USA: Dassault Systèmes; 2018.

[31] Nielsen JCO. High-frequency vertical wheel–rail contact forces – Validation of a prediction model by field testing. Wear 2008;265(9–10):1465–71.

[32] Iwnicki S. Manchester benchmarks for rail vehicle simulation. Veh Syst Dyn 1998;30(3–4):295–313.

[33] Aggestam E, Nielsen JCO, Bolmsvik R. Simulation of vertical dynamic vehicle–track interaction using a two-dimensional slab track model. Veh Syst Dyn 2018;56(11):1633–57.

[34] Plos M, Shu J, Zandi K, Lundgren K. A multi-level structural assessment strategy for reinforced concrete bridge deck slabs. Struct Infrastruct Eng 2017;13(2):223–41.

[35] Al-Emrani M, Engström B, Johansson M, Johansson P. Bärande konstruktioner – Del 2 [Supporting structures – Part 2, in Swedish]. Tech. rep., Gothenburg, Sweden: Department of Civil Engineering and Environmental Engineering, Chalmers University of Technology; 2011, p. 1–320.

[36] Engström B. Restraint cracking of reinforced concrete structures. Tech. rep., Gothenburg, Sweden: Department of Civil Engineering and Environmental Engineering, Chalmers University of Technology; 2014, p. 1–165.

[37] Jaccoud J-P. Cracking under long term loads or imposed deformations. CEB Comité Euro Int Béton Bull 1997;143–55.

[38] Correa N, Oyarzabal O, Vadillo EG, Santamaria J, Gomez J. Rail corrugation development in high speed lines. Wear 2011;271(9–10):2438–47.

[39] EN 13848-6 CEN Standard. Railway applications – Track – Track geometry quality – Part 6: Characterisation of track geometry quality. 2014.

[40] Claus H, Schiehlen W. Modeling and simulation of railway bogie structural vibrations. Veh Syst Dyn 1998;29(S1):538–52.

[41] Hult J. Bära brista: Grundkurs i hållfasthetslära [Basic course in strength of materials, in swedish]. Almqvist and Wiksell; 1979.

[42] Berggren E. Railway track stiffness: Dynamic measurements and evaluation for efficient maintenance (Ph.D. thesis), Stockholm, Sweden: Department of Aeronautical and Vehicle Engineering, Royal Institute of Technology (KTH); 2009.

[43] Hjulsbro Steel AB. Environmental product declaration (EPD) – PC-strand – Prestressed steel for reinforcement of concrete (single supplier). 2020.